

Stalk-mediated communication in the dynein motor domain

Stefan Niekamp¹, Nicolas Coudray^{2,3}, Nan Zhang¹, Ronald D. Vale¹ & Gira Bhabha^{2*}

¹ Department of Cellular and Molecular Pharmacology and Howard Hughes Medical Institute, University of California, San Francisco, 600 16th Street, San Francisco, CA 94158.

² Skirball Institute of Biomolecular Medicine, New York University School of Medicine, New York, NY 10016

³ Applied Bioinformatics Laboratories, New York University School of Medicine, New York, NY 10016

* Corresponding author: gira.bhabha@gmail.com

Abstract

The movement of a molecular motor protein along a cytoskeletal track requires communication between the ATPase and polymer-binding sites. While these sites are located in close proximity in kinesin and myosin, dynein has a ~135 Å coiled-coil stalk that separates the microtubule-binding domain (MTBD) from the AAA ATPase ring. An analysis of 534 unique dynein sequences revealed that the length of the stalk is highly conserved. A panel of mutants based on our analysis revealed three regions of the stalk for which altering the length resulted in diffusional motion along microtubules. Two diffusive mutants also showed hyperactive ATPase activity, and were no longer sensitive to microtubules. Structural analysis of one of these mutants using cryo electron microscopy revealed a previously uncharacterized open conformation of the AAA ring. This conformation is lowly populated in the wild-type protein and thus may be an on-pathway catalytic intermediate. Our results reveal how changes in the stalk can affect the conformation and activity of the AAA ring, and modulate dynein motility.

Dyneins are minus-end directed, microtubule-based molecular motors that belong to the AAA+ (ATPases associated with diverse cellular activities) superfamily of proteins. Cytoplasmic dynein is responsible for the transport of numerous cargoes along microtubules (MTs), such as organelles, vesicles, viruses, and mRNAs^{1,2}. In addition, cytoplasmic dynein plays key roles in facilitating basic cell biological processes such as spindle positioning during mitosis³. Mutations and defects in cytoplasmic dyneins are associated with many diseases such as neurodegenerative diseases and cancers⁴.

The cytoplasmic dynein holoenzyme is composed of two identical ~500 kDa heavy chains and multiple associated polypeptide chains that primarily bind to the N-terminal tail of dynein⁵. Regulatory proteins such as Lis1 and NudE bind to some dyneins and can modify its motility properties^{6,7}. To initiate processive motility for cargo transport, human cytoplasmic dynein also requires dynactin as well as cargo-adaptor proteins such as BicD and Hook3^{8,9}. However, the core element for motility of all dyneins lies in the conserved motor domain of the heavy chain, which consists of six different AAA domains that are linked together as an asymmetric hexameric ring (AAA1-AAA6). Only AAA1-AAA4 can bind nucleotides¹⁰⁻¹⁶ (**Fig. 1 a**); ATP hydrolysis in AAA1 is required for dynein stepping and AAA3 acts as a switch that facilitates robust motility when ADP is bound¹⁷⁻¹⁹. The catalytic domains in the AAA ring are spatially distant from the microtubule binding domain (MTBD); the two are connected via the coiled-coil “stalk” that emerges from AAA4. Another coiled-coil element, called the buttress, protrudes from AAA5 and interacts with the stalk close to the ring (**Fig. 1 a**); the buttress also has been shown to be important for the allosteric communication between ring and MTBD¹³. The N-terminal linker, which lies on top of the ring, is believed to serve as a mechanical element that drives motility¹⁰. Over the last few years, several structural studies have illuminated a series of conformational changes in the dynein AAA ring during the ATPase cycle^{11-13,18}. The key conformational changes include domain rotations within the AAA ring, and rearrangements of the linker domain.

To coordinate motility, motor proteins must communicate between the ATPase and polymer binding sites. In the case of kinesin and myosin, the ATPase and track binding sites are located relatively close to each other in the same domain²⁰, whereas in dynein, the ATPase and track-binding sites are far apart from each other. ATP binding to AAA1 results in a weakened affinity ($K_d > 10 \mu\text{M}$) of the motor for microtubules (MTs). After ATP hydrolysis, the motor binds MTs with stronger affinity ($K_d < 1 \mu\text{M}$)²¹. In this way, the AAA ring controls the affinity of the MTBD for MTs. Conversely, interaction of the MTBD with MTs regulates the

ATPase activity in the AAA ring²¹. How this allosteric communication occurs is still poorly understood. The conundrum is that the very small, ~10 kDa microtubule-binding domain is spatially separated from the AAA ring by the ~135 Å long coiled-coil stalk²¹⁻²⁵. Furthermore, the stalk is positioned between AAA4 and AAA5, which is on the opposite side of the ring from AAA1, making the distance between the main catalytic site and the MTBD ~240 Å.

To enable two-way communication between the MTBD and AAA ring to work, it has been suggested that the stalk undergoes conformational changes^{21,26,27}. One hypothesis is that sliding between the two anti-parallel helices of the stalk coiled-coil leads to different microtubule affinities; the stalk in the β + registry results in a low MT affinity state and the α registry results in high MT affinity^{21,23}. This is further supported by structural work which has shown that when ADP.Vi is bound to AAA1, coiled-coil 2 (CC2) of the stalk is kinked and slides together with the buttress relative to coiled-coil 1 (CC1)¹². Another study speculates that local melting of the coiled-coil between different states of the hydrolysis cycle plays a major role in the communication^{28,29}.

To gain better insights into the mechanism by which the stalk transmits information from the AAA ring to the MTBD, we have identified mutants in the dynein stalk that block communication between the ATPase and microtubule binding sites. These mutants show diffusive movement along MTs and also hydrolyze ATP at maximal rates in a microtubule-independent manner. Structural characterization by cryo EM of one mutant reveals a stabilization of a previously uncharacterized open conformation of the AAA ring. These results provide insight into how mutations in specific locations of the stalk can affect the conformational changes and ATPase activity of the AAA ring.

Results

The coiled-coil stalk of the dynein motor domain is strikingly conserved in length

To better understand dynein's coiled-coil stalk, we obtained a dataset of 677 unique dynein heavy chain sequences from 229 fully sequenced eukaryotic genomes including sequences from cytoplasmic, axonemal and IFT dyneins (see Methods). Since our analysis was focused on the motor domain and in particular on the stalk, we pruned our data set (**Supplementary Note 1**), and aligned 534 motor domain sequences using MAFFT^{30,31}.

We defined boundaries of CC1 and CC2 of the stalk using anchor residues that are very well conserved: P2989 and P3101 define CC1, and P3228 and Y3333 define CC2 (**Fig. 1 a**, residue numbers here and throughout the manuscript correspond to yeast cytoplasmic dynein, unless otherwise specified). Strikingly, we noticed that the length of CC1 and CC2 are extremely conserved: 501 out of 534 sequences have exactly 115 residues in CC1 and 506 out of 534 sequences have exactly 106 residues in CC2 (**Fig. 1 b, c**). The length and size of other subdomains of the dynein motor domain are not as well conserved (**Supplementary Fig. 1 a, b**). Surprisingly, despite the conservation of length, the primary sequence of the stalk is not particularly well conserved (**Supplementary Fig. 1 c, d**). We also investigated other features such as hydrophobicity and charge variation but no clear patterns of conservation were observed in the stalk (**Supplementary Fig. 1 e-g**).

Our initial analysis revealed a handful of sequences that varied in length from 115 residues in CC1 and 106 residues in CC2 (**Fig. 1 b, c**). Coiled-coils contain a repeating pattern of 7 residues (heptad repeat) consisting of charged and hydrophobic residues. The hydrophobic stretch of the heptad repeat in one coil interacts with the hydrophobic region of the heptad repeat on the other coil, thus generating a stable coiled-coil. Based on the conserved structural motifs in the coiled-coil, one may expect that, for example, a deletion of 7 residues in CC1 would correspond to a deletion of 7 residues in CC2, in order to maintain the interaction between the two coils. Indeed, previous work has shown that insertions and deletions of the same number of residues in both sides does not alternate velocity and ATPase activity significantly²⁵. Surprisingly, however, the variants in our dataset contained either insertions or deletions in one of the coils, but not in both simultaneously.

Stalk mutants show nucleotide-independent diffusion

To investigate how insertions and deletions in the stalk affect dynein's motility, we made a panel of 18 insertion and deletion mutants in the yeast cytoplasmic dynein background, which covered an extensive region of the stalk (**Fig. 1 d, Supplementary Note 1, Supplementary Fig. 2, 3 and Supplementary Table 1**).

Previous studies have shown that the yeast dynein motor domain artificially dimerized via a GST-dimer moves processively along microtubules in a manner that is similar to the intact dynein holoenzyme^{32,33}. We expressed and purified GST-dimerized versions of each mutant with an N-terminal GFP, and used single molecule total internal reflection fluorescence (TIRF) microscopy assays^{32,34} for initial characterization of single molecule motility.

Our panel of mutants displayed a wide variety of phenotypes (**Fig. 2 a-c, Supplementary Fig. 4 a**). In several locations, insertions and deletions can be tolerated without any effect on motility, suggesting that these regions can vary in length without affecting the motor (**Fig. 2a, Supplementary Note 2**). As expected, mutations in the region of the stalk-butress interaction cannot be tolerated and result in a dead motor (**Fig. 2 d**). Three mutants (**Fig. 3 a**) from our panel (mutants 2, 5, and 13) presented a diffusive-like behavior, with single molecules randomly moving back-and-forth along the microtubule (**Fig. 2, Supplementary Movies 1-4**). Surprisingly, in the absence of ATP, we saw very similar diffusive-like behavior for all three mutants, suggesting that mutant 2, mutant 5, and mutant 13 are not rigor-bound to microtubules, as it is the case for wild-type protein (**Fig. 3 b, c, Supplementary Fig. 5 a-h, Supplementary Movies 5-8**). Hence, we conclude that the movement of mutant 2, mutant 5, and mutant 13 is diffusive (**Fig. 3 d**).

To assess the ensemble activity of these mutants, we tested them in a microtubule gliding assay in which monomeric dyneins (wild-type or mutants) were attached to a glass coverslip. In the presence of active motor, the microtubules glide across the surface, driven by an ensemble of dynein motors attached along the length of the microtubule. Results from this assay show that the three mutants generated microtubule gliding, although their velocities were ~10-fold lower than wild-type dynein (**Fig. 4 , Supplementary Movies 9-12**). In order to determine whether the microtubules were moving in the same direction as for wild-type dynein, our gliding assay also included single molecules of a human homodimeric kinesin-1 (K490)³⁵ that move processively towards the plus end of the microtubule (**Fig. 4 a**). By observing the direction of kinesin movement, we could mark the plus and minus ends of the microtubule and

assess their direction of gliding movement driven by the dynein movement. Our results showed that the direction of mutant 2, 5 and 13 microtubule gliding was the same as for wild-type dynein.

In conclusion, mutants 2, 5, and 13 show nucleotide-independent diffusive movement as single molecules, while ensembles of these motors can produce weak directional movement.

Diffusive mutants show microtubule-independent hyperactive ATP hydrolysis

We next measured the ATPase activity of mutant 2, mutant 5, and mutant 13 in the absence or presence of microtubules. Wild-type dynein had a basal ATPase turnover of 0.75 ± 0.34 ATP/motor/sec, which increased with increasing concentrations of microtubules to a k_{cat} of 15.18 ± 1.18 ATP/motor/sec and K_m of $0.50 \pm 0.17 \mu M$ for tubulin (**Fig. 5 a**). These ATPase values are similar to those previously reported^{15,25,36} (**Supplementary Table 2**). In contrast, the three diffusive mutants showed high basal ATPase activity that was not responsive to increasing microtubules concentration. Interestingly, the basal ATPase activities of mutants 5 and 13 were very similar to the maximal microtubule-stimulated ATPase activity of the wild-type protein (**Fig. 5 a, b, Supplementary Table 3**). These results indicate that the diffusive mutants are defective in microtubule regulation of ATPase activity.

Next, we sought to examine whether nucleotide can regulate the binding affinity of dynein to microtubules using a cosedimentation assay. In wild-type dynein, the motor binds tightly to microtubules in the absence of ATP, but weakly in the presence of ATP (**Fig. 5 c**). In contrast to nucleotide-dependent microtubule-affinity of the wild-type enzyme, the microtubule affinity of the mutants was low in the absence of nucleotide and in the presence of ATP or AMPPNP (**Fig. 5 d-f, Supplementary Table 4**).

Structural basis for hyperactivity of mutant 5

We next sought to understand the structural basis underlying the uncoupling between the microtubule and ATPase sites in the diffusive mutants. Because of its high basal ATPase activity, we decided to focus on mutant 5. First, we used a negative stain electron microscopy (EM) based assay with the goal of assessing the linker conformation and/or flexibility. We previously were able to identify distinct linker conformations using 3D classification and

refinement from negative stain EM data¹⁸. For this assay, we used the ATP analog AMPPNP to mimic an ATP-bound state of the enzyme, in which the linker in the wild-type enzyme is straight and docked to the AAA ring at AAA5. 3D classification and refinement of negative stain EM data of mutant 5 showed weaker density for the N-terminal region of the linker, suggesting that the position of the linker in mutant 5 may be more flexible than the wild-type (**Supplementary Fig. 6 a-d**). More strikingly, however, we observed a “gap” (missing density) in the ring, at the region of AAA5 (**Supplementary Fig. 6 b**).

To obtain more information about the gap in the AAA ring, we collected a cryo EM dataset of mutant 5 in the presence of 2 mM AMPPNP. After 3D classification and refinement, we identified two distinct classes. Our cryo EM reconstructions for both classes are at ~7.5-8 Å resolution (**Supplementary Fig. 7 a, b**), where we can confidently model domain motions, but not secondary structure. Therefore most of our analysis is focused on subdomain movements within the AAA ring. Each AAA domain consists of a large subdomain (AAAL) and a small subdomain (AAAs), which can be considered as rigid bodies in the context of our resolution. AAAL and AAAs subdomains from each AAA domain were fit simultaneously into our density maps for each conformation to generate a model corresponding to each map.

The majority of particles (~71% of all particles, 7.7 Å resolution) adopt what we refer to as the class 1 conformation. This reconstruction shows a similar “gap” that we observed by negative stain (**Fig. 6 a, b**). At the higher resolution, the gap can be clearly identified as a rearrangement between the small and large domains of AAA5. In addition, density for most of the distal stalk as well as the buttress is missing, indicating flexibility in these regions. For the second class from our 3D classification, class 2, the minor conformation (~29% of all particles, 7.6 Å resolution), the cryo EM map shows a closed ring with no gap between the small and large domain of AAA5; the helices of the initial part of the stalk and for buttress also well defined (**Fig. 6 a**). The density for the helices of the buttress show that there is a small change in the buttress conformation relative to the AMPPNP-bound dynein crystal structure (PDB 4W8F) (**Supplementary Fig. 7 c**). An additional and more subtle difference between class 1 and 2 density is found in the N-terminal GFP tag. In contrast, for class 1 (major class with “open” ring), the density for the N-terminal GFP tag is not well defined (**Supplementary Fig. 7 d-e**). This may indicate that the N-terminus of the linker is also more flexible in this class, and potentially not docked as well onto the ring.

When the models for class 1 and class 2 are aligned on the AAA1L domain, AAA6s and AAA1L are anchored as a single unit, while the gap between AAA5L and AAA5s results in

domain movements around the rest of the ring (**Fig. 6 c, d, Supplementary Fig. 7 f-p**), including rearrangements between AAA2L and AAA2s. Domain movements between class 1 and class 2 are largely clam-shell movements in each domain (**Supplementary Movie 13**), resulting in radial expansion and contraction of the ring. In contrast, comparing movements between class 1 and the ADP-vanadate state of dynein¹² shows clockwise rotation of the domains that results in a compact ring primed for hydrolysis, as previously described (**Supplementary Figure 7 q, r**). In both class 1 and class 2, AAA2L is positioned away from the active site of AAA1, and the ring is therefore not primed for hydrolysis. A comparison of class 1 and class 2 with Apo (PDB 4AKG), ADP-Vi (PDB 4RH7) and ADP (PDB 3VKG) states show that in class 1, the ring is even more relaxed than in the Apo state, probably due to the stalk and buttress not being engaged with each other (**Supplementary Movie 14**).

Discussion

Mutations in the stalk disrupt communication between AAA ring and MTBD

Given the spatial separation between dynein's catalytic AAA ring and the MTBD, it is apparent that allosteric communication must be mediated in some way via the stalk. In comparing more than 500 sequences of dynein's motor domain we found that the length of the stalk is remarkably well conserved among species and types of dynein, such as cytoplasmic, axonemal and IFT dynein. From our initial analysis, only approximately 5% have insertions or deletions in CC1 or CC2. It is worth noting that since the analysis was carried out, several sequences have been replaced with newer corrected sequences which do not contain these insertions/deletions, suggesting that in reality closer to 1% of sequences deviate from the conserved stalk lengths (**Supplementary Fig. 1 h-i, Supplementary Table 1, Supplementary Note 3**). Interestingly, the wild-type protein sequences on which we based our mutants that showed diffusive movement have been updated in the databases and do not show any insertions or deletions anymore. Based on currently available sequences, most likely dyneins with this phenotype do not exist; however, we serendipitously stumbled upon these insertions and deletions in regions of the stalk, which do mediate communication between the AAA ring and MTBD, and these mutations shed light on the dynein motility mechanism.

Three of our mutants, mutant 2, mutant 5, and mutant 13 show nucleotide-independent diffusion. A microtubule stimulated ATPase assay revealed that all three mutants hydrolyze ATP independently of microtubule concentration and that two of these mutants are hyperactive and have a basal activity that is as high as the maximal turnover rate in the wild-type protein. Our cryo EM structure revealed that the buttress in this mutant is much more flexible than in the wild-type protein, and likely the buttress-stalk interaction is compromised. Consistent with this idea, a mutation in the buttress region of dictyostelium dynein also results in a mutant with high basal ATPase activity²¹. Our data point to three specific locations in the stalk that are important for mediating communication between the MTBD and the AAA ring, and likely the length of these regions is critical for maintaining this communication. The position within the coiled-coil, and the size of insertion or deletion impact the motility properties of dynein (**Fig 2, Supplementary Note 2**). It is likely that there are many more hotspots in the stalk that remain to be discovered, and further work will be necessary to understand exactly what structural

changes occur in the stalk itself as information is transmitted in both directions between the AAA ring and the MTBD.

A model for communication between the AAA ring and MTBD

Comparing and combining these results with previous work, our data suggest that mutant 2, 5 and 13 trapped the stalk in a state that results in low affinity of the MTBD for microtubules. This likely enables diffusive movement of the motor along the microtubule independent of ATP concentration. Our structural data for mutant 5 augments our understanding of and puts a new perspective on the conformational changes in the AAA ring of dynein during the hydrolysis cycle (**Fig. 7**).

We have previously characterized the AMPPNP-bound wild-type dynein motor domain by negative stain EM and crystallography¹⁸. In the previous work, we used 3D classification to sort our data, and found that the reconstruction from the major class of particles agreed very well with the crystal structure within the scope of our resolution. However, we had also obtained a smaller subset of particles (17% of the total), in which the motor domain was in a somewhat different conformation. Specifically, the linker density was weaker at the N-terminus of the linker, as well as in the AAA5 region, in which our mutant shows a clear “gap”. (**Fig. 6, Supplementary Fig. 7**). While we were unable to interpret this minor class in the previous work, the results for mutant 5 put these data in a new light. Since we observe a small population of particles for WT dynein:AMPPNP that resemble the major class of particles in our mutant, we propose that this new conformation with an “open” ring may be an on-pathway intermediate in the catalytic cycle, and that our mutant has stabilized this conformation. In the mutant, the previously higher energy state is now the ground state. Indeed, in keeping with this, when we analyze previously deposited data for the motor domain in the presence of ATP (**Supplementary Fig. 6 e, f**, EMDB: 6065-6068), we observe classes in which a similar “gap” in density around AAA5 is seen.

Based on previous findings^{18,19}, it is clear that in order for ATP hydrolysis to proceed, the linker must be undocked from the ring, to allow full closure of AAA2L and correct positioning of the arginine finger that promotes ATP hydrolysis, and that there is a key change in interaction of the stalk and buttress that accompanies this conformational change in the ring. The movement of the buttress is coupled to CC2 of the stalk, but it slides relative to CC1¹². Both the linker docking and likely the stalk buttress interaction provide some regulation, or,

“put the brakes on” conformational changes in the ring. The “gap” we observe in the AAA ring in mutant 5 suggests that these mutations potentially also disrupted the stalk/buttress interaction. It is likely that this is an “extension” of the change in buttress-stalk interaction observed by Carter and colleagues in the dynein structure bound to ADP and vanadate (PDB code: 4RH7). We propose that mutant 5 (and potentially mutant 13) stabilizes a minor, on-pathway conformation in dynein’s ATP hydrolysis cycle in which the ring is significantly more “open”, linker docking to the ring is potentially weaker, and ATP hydrolysis is accelerated. It is possible that the “gap” generated between AAA5L and AAA5s may facilitate the conformation observed in the ADP-Vi state (PDB 4RH7) (**Supplementary Movie 14**). Previously reported buttress mutations that presumably disrupt the stalk-buttress interaction¹³ showed very similar ATPase activity to our mutants 5 and 13. In this case, basal ATPase rates were similarly high, and also microtubule independent.

Taken together, our data suggest that the mutants have disrupted two-way communication between the MTBD and the AAA ring. At least three regions of the stalk are important for mediating allosteric communication in the dynein motor domain. These mutations also resulted in a non-directional, diffusive motor with unregulated ATPase activity, suggesting that the communication they mediate is crucial for dynein motility. Cryo EM data of mutant 5 stabilized an open conformation of the ring that was previously present and observed at low resolution as a minor conformation in wild-type dynein. We propose that this new conformation of the AAA ring is a transient on-pathway intermediate in the dynein mechano-chemical cycle.

Online methods

Bioinformatic analysis. The detailed process is described in **Supplementary Note 1**. Briefly, we used 677 unique axonemal and cytoplasmic dynein heavy chain sequences from 229 fully sequenced eukaryotic genomes, which we received from Christian Zmasek, [Godzik lab](#), Burnham. This data set was pruned based on well defined criteria as listed in **Supplementary Note 1** and analyzed using Jalview³⁷. Remaining sequences were aligned using MAFFT³⁰ in the Bioinformatic Toolkit³¹ and mutations in the stalk were manually identified by comparing sequences in Jalview. All alignment files are available as **Supplementary Material**.

Yeast strains. Recombinant *S.cerevisiae* cytoplasmic dynein (Dyn1) truncated at the N-terminus (1219-4093 aa) was used in this study. All constructs used in this study are listed in **Supplementary Table 1**. Dimeric constructs are based on VY208 and were created by artificially dimerization through an N-terminal GST-tag³² and tagged with a HaloTag (Promega) at the C-terminus as well as a GFP at the very N-terminus. Monomeric constructs (VY137) are GFP tagged at the N-terminus. Stalk mutations were inserted by homologous recombination as previously described³².

Protein expression and purification. Dynein was expressed and purified as previously described³². Monomeric and dimeric constructs were further purified by gel filtration on a GE Healthcare Superdex 200 10/300GL and a GE Healthcare Superose 6 10/300GL column, respectively in dynein gel filtration buffer (50 mM K-Ac, 20 mM Tris, pH 8.0, 2 mM Mg(Ac)₂, 1 mM EGTA, 1 mM TCEP, and 10% glycerol) and flash frozen afterwards. The ‘cysteine-light’ human ubiquitous kinesin-1 dimer E215C K490 construct was cloned and purified as previously described^{38,39}. Following dialysis the E215C K490 construct was reacted for 4 h at 4°C with Cy3-maleimide (GE Healthcare, PA13131) at a motor/Cy3 dye ratio of 1:10 as previously described³⁹. The unreacted maleimide dyes were then quenched with 1 mM dithiothreitol (DTT). Afterwards the kinesin was purified by gel filtration over a S200 10/300GL column (GE Healthcare) in kinesin gel filtration buffer (25 mM Pipes (pH 6.8), 2 mM MgCl₂, 200 mM NaCl, 1 mM EGTA, 1 mM DTT, and 10% sucrose) and then flash frozen.

Microtubule preparation. Tubulin was purified and polymerized as previously described⁸. For single molecule motility assays unlabeled tubulin, biotinylated tubulin, and fluorescent tubulin were mixed at an approximate ratio of 20:2:1 in BRB80 (80 mM Pipes (pH 6.8), 1 mM EGTA, and 1 mM MgCl₂). For the gliding assay unlabeled tubulin and fluorescent tubulin were mixed at an approximate ratio of 20:1 in BRB80. For tubulin that was used in the ATPase assay as well as the microtubule affinity assay only unlabeled tubulin was used. We added 1 mM GTP to all polymerization reactions. Then the mixtures were incubated for 15 min in a 37°C water bath. 20 µM of Taxol (Sigma, T1912) was then added and the mixture was incubated for 2 more hours at 37°C. Before usage, microtubules were spun over a 25% sucrose cushion in BRB80 at ~160,000 g for 10 min in a tabletop centrifuge.

Gliding and single molecule motility assay. We made custom flow chambers using laser-cut double-sided adhesive sheets (Soles2dance, 9474-08x12 - 3M 9474LE 300LSE). We used glass slides (Thermo Fisher Scientific, 12-550-123), and coverslips (Zeiss, 474030-9000-000). We cleaned the coverslips in a 5% v/v solution of Hellmanex III (Sigma, Z805939-1EA) at 50°C overnight and then washed them extensively with Milli-Q water. The flow-cells were assembled in a way that each chamber holds approximately 10 µl.

Every data collection was carried out at room temperature (~23 °C) using a total internal reflection fluorescence (TIRF) inverted microscope (Nikon Eclipse Ti microscope) equipped with a 100× (1.45 NA) oil objective (Nikon, Plan Apo λ). We used an Andor iXon 512x512 pixel EM camera, DU-897E and a pixel size of 159 nm. Dynein (always as dimer and either labeled with GFP only or with GFP and a Halo488 dye (Promega, G1001)) was excited with a 488 nm laser (Coherent Sapphire 488 LP, 150 mW), kinesin with a 561 nm laser (Coherent Sapphire 561 LP, 150 mW), and microtubules with a 640 nm laser (Coherent CUBE 640-100C, 100 mW). For the gliding assay, images were recorded with 100 ms exposure time and a 2 sec frame rate for MTs and a 100 msec frame rate for kinesin. For the single molecule assay of dynein, we used 100 msec exposures and a 2 sec frame rate and a 100 msec frame rate for kinesin. The acquisition software was µManager⁴⁰ 2.0 and data was analyzed in ImageJ⁴¹.

For the gliding assay, we first added 10 µl of GFP antibody (Abcam, ab1218) and incubated for 5 min. Then we washed with 20 µl of DAB with 2 mg/ml β-casein and 0.4 mg/ml κ-casein. We then added 10 µl of dynein and incubated for another 5 min which was followed by an additional wash with 20 µl of DAB with 2 mg/ml β-casein and 0.4 mg/ml κ-casein. Next, we added 10 µl of polymerized microtubules and incubated for 5 min. Then we washed with 30

μ l of DAB with 2 mg/ml β -casein and 0.4 mg/ml κ -casein. Finally, 10 μ l of DAB with kinesin, 0.4 mg/ml κ -casein, 10 μ M Taxol, 1 mM Mg-ATP, and the PCA/PCD/Trolox oxygen scavenging system⁴² was added.

Prior to the single molecule motility assays dynein was labeled with Halo488 dye (Promega, G1001) as previously described¹⁸. Briefly, dynein constructs were mixed with 20 μ M Halo Alexa488 dye and incubated on ice for 10 min and a PD MiniTrap G-25 column (GE Healthcare) equilibrated with dynein gel filtration buffer was used to remove excess dye afterwards.

The flow chambers for the single molecule motility assay were prepared as previously described³⁴. Briefly, we first added 10 μ l of 5 mg/ml Biotin-BSA in BRB80 and incubated for 2 min. Then we washed with 20 μ l of BRB80 with 2 mg/ml β -casein (Sigma, C6905), 0.4 mg/ml κ -casein (Sigma, C0406). Afterwards we added 10 μ l of 0.5 mg/ml Streptavidin in PBS for a 2 min incubation. Next, we again washed with 20 μ l of BRB80 with 2 mg/ml β -casein, and 0.4 mg/ml κ -casein. This was followed by the addition of 10 μ l of polymerized microtubules and a 5 min incubation. Then we washed with 30 μ l of DAB (50 mM K-Ac, 30 mM HEPES, pH 7.4, 2 mM Mg(Ac)₂, 1 mM EGTA) with 2 mg/ml β -casein, 0.4 mg/ml κ -casein, and 10 μ M Taxol. Finally we added 10 μ l of dynein and kinesin in DAB with 0.4 mg/ml κ -casein, 10 μ M Taxol, 1 mM Mg-ATP, and the PCA/PCD/Trolox oxygen scavenging system⁴². In the single molecule assay where ATP was omitted, the final solution contained 10 μ l of dynein in DAB with 0.4 mg/ml κ -casein, 10 μ M Taxol, and the PCA/PCD/Trolox oxygen scavenging system⁴².

ATPase assay. The ATPase assays were carried out in DAB (50 mM K-Ac, 30 mM HEPES, pH 7.4, 2 mM Mg(Ac)₂, 1 mM EGTA) as follows. We mixed dynein (monomeric for all constructs) to a final concentration of 10-20 nM with 2 mM Mg-ATP (Sigma), 0.2 mM NADH (Sigma), 1 mM phosphoenolpyruvate (Sigma), 0.01 U pyruvate kinase (Sigma), 0.03 U lactate dehydrogenase (Sigma), 10 μ M Taxol, 1 mM DTT, and 0-5 μ M microtubules in DAB. Absorbance at 340 nm was continuously measured in an Eppendorf Spectrophotometer (UV-Vis BioSpectrometer) and the data was fit to the following equation¹⁸ using an excel curve fitting routine:

$$k_{obs} = (k_{cat} - k_{basal}) \frac{[MT]}{K_M + [MT]} + k_{basal}.$$

Microtubule affinity assay. The microtubule affinity assays were carried out in DAB (50 mM K-Ac, 30 mM HEPES, pH 7.4, 2 mM Mg(Ac)₂, 1 mM EGTA) as follows. We mixed dynein (monomeric for all constructs) to a final concentration of approx. 50 nM with 10 μ M Taxol, 1

mM DTT, and 0-8 μ M microtubules in DAB. For the measurements with ATP we added 5 mM Mg-ATP (Sigma) and for the experiment with AMPPNP we added 5 mM Mg-AMPPNP (Sigma). After a 3 min incubation at room temperature the samples were spun over a 25% sucrose cushion in DAB at $\sim 160,000 g$ for 10 min in a tabletop centrifuge. The concentration of dynein in the supernatant (unbound) and in the pellet (bound) was determined by measuring the intensity of the N-terminal GFP on a Typhoon (GE Healthcare) and the data was fit to the following equation using an excel curve fitting routine: $k_{obs} = (B_M - k_{basal}) \frac{[MT]}{K_d + [MT]} + k_{basal}$ (B_M maximum binding, K_d dissociation constant).

EM data collection. For negative stain, data for mutants 5 (monomer) was collected on a Tecnai F20 microscope with a Tietz F416 CMOS detector at the New York Structural Biology Center (NYSBC). Leginon software⁴³ was used for the semi-automated collection of 825 images at a magnification of x62,000 and a pixel size of 3 Å per pixel. For cryo EM data collection, 1200 movies of mutant 5 (monomer) were recorded with SerialEM⁴⁴ at 300 kV on a Titan Krios (FEI) equipped with a K2 summit camera (Gatan) at 0.655 Å per pixel in super-resolution mode at Janelia Research Campus.

EM data processing. For the images of the negatively stained sample, particles were selected using DoG picker⁴⁵ in APPION⁴⁶, then extracted in Relion 2.1.0⁴⁷ into boxes of 180x180 pixels, leading to 156,199 boxes for mutant 5. A round of 2D classification was performed to remove junk and noisy particles, leading to 54,913 particles selected. Subsequent image processing steps were carried out using CryoSPARC⁴⁸. After having generated an ab-initio model, those particles were used to generate eight 3D classes. Because of the similarity between all those classes, a final round of 3D refinement was completed using all of the particles. For the cryo-EM images, the movies were first aligned and binned to 1.31 Å per pixel with MotionCor2 v1.0.5⁴⁹, and then the contrast transfer function parameters were estimated with GTCF 1.06⁵⁰. The particles were picked automatically in Relion 2.1.0⁴⁷ using a Gaussian blob as a reference and further processing was done in CryoSPARC⁴⁸. Out of the 310,085 regions automatically picked, 136,056 were kept after evaluation of 2D classes. Two ab-initio models were first generated in CryoSPARC, and the best one was used in a 4-class 3D heterogeneous refinement. Then, two 3D homogeneous refinements were completed: one with class 3 (here referred to as class 2 - with 29% of remaining particles and with a resolution of 7.6 Å), and another one (here referred to as class 1 - with 71% of remaining particles and with a resolution

of 7.7 Å) with the three other classes which looked very similar and were therefore combined before refinement. The final maps were then filtered for display using a B-factor of -400. For modelling, we used PDB 4W8F as a reference. The PDB file was split it in into 13 domains (small and large subdomains for each AAA domain, and the linker) and, for each of those domains, we simultaneously fit all 13 subdomains into the map Chimera⁵¹. We noticed that the rigid body of the buttress region in class 2 map did not perfectly fit the densities (**Supplementary Fig. 7 c**). This model was therefore subjected to the `real_space_refine` algorithm in PHENIX⁵² using 2 cycles and 100 iterations to optimize the fit. Figures and movies were generated with the UCSF Chimera package or the Pymol Molecular Graphics System (version 2.0, Schrödinger, LLC) .

Figure preparation. Figures and graphs were created using Pymol (version 2.0 Schrödinger, LLC) and Chimera⁵¹ (structure representation, ImageJ⁴¹ (light microscopy data), Jalview³⁷ (sequence analysis and representation), Affinity designer(version 1.6.1, Serif (Europe) Ltd) and Python (version 2.7, Python Software Foundation).

Statistics. For each result obtained, the inherent uncertainty due to random or systematic errors and their validation are discussed in the relevant sections of the manuscript. Details about the sample size, number of independent calculations, and the determination of error bars in plots are included in the figures and figure captions.

Data availability. EM data for the structures were deposited in the Electron Microscopy Data Bank under accession codes EMD-7829 (Class 1) and EMD-7830 (Class 2). The sequence alignment files used to create the mutants are available as **Supplementary Material**. All other data are available from the corresponding authors upon request.

Life Sciences Reporting Summary. Further information on experimental design is available in the Life Sciences Reporting Summary.

Acknowledgements

We would like to thank Christian Zmasek, [Godzik lab](#), Burnham for the initial sequence alignment file. For the light microscopy experiments, we thank Nico Stuurman and Walter Huynh for assistance in microscope operation and advice. We thank Kelsey Jordan at the New York Structural Biology Center for assistance with data collection of negatively stained samples. For cryo-EM, we thank Hui-Ting Chou and Zhiheng Yu at the HHMI Janelia Farm Research Campus for assistance in microscope operation and data collection. For EM data processing, this work has utilized computing resources at the High-Performance Computing Facility at NYU Langone Medical Center. We thank Martin Ossowski and his HPC team as well as Joe Katsnelson for EM data processing support. The authors gratefully acknowledge funding support from the NIH National Institute of General Medical Sciences: R00GM112982 (G.B.), R01GM097312 (R.D.V.), Damon Runyon Cancer Research foundation DFS-20-16 (G.B.), Howard Hughes Medical Institute (R.D.V.) and the UCSF Discovery Fellowship (S.N.). Some of this work was performed at the Simons Electron Microscopy Center and National Resource for Automated Molecular Microscopy located at the New York Structural Biology Center, supported by grants from the Simons Foundation (349247), NYSTAR, and the NIH National Institute of General Medical Sciences (GM103310).

Author Contributions

G.B., S.N. and R.D.V. conceived the research. G.B., S.N., N.C. and N.Z. performed experiments and collected data. G.B., S.N., N.C. and R.D.V. analyzed data. G.B. and S.N. wrote the manuscript. All authors edited the manuscript.

Competing interests

The authors declare no competing financial interests.

Figures

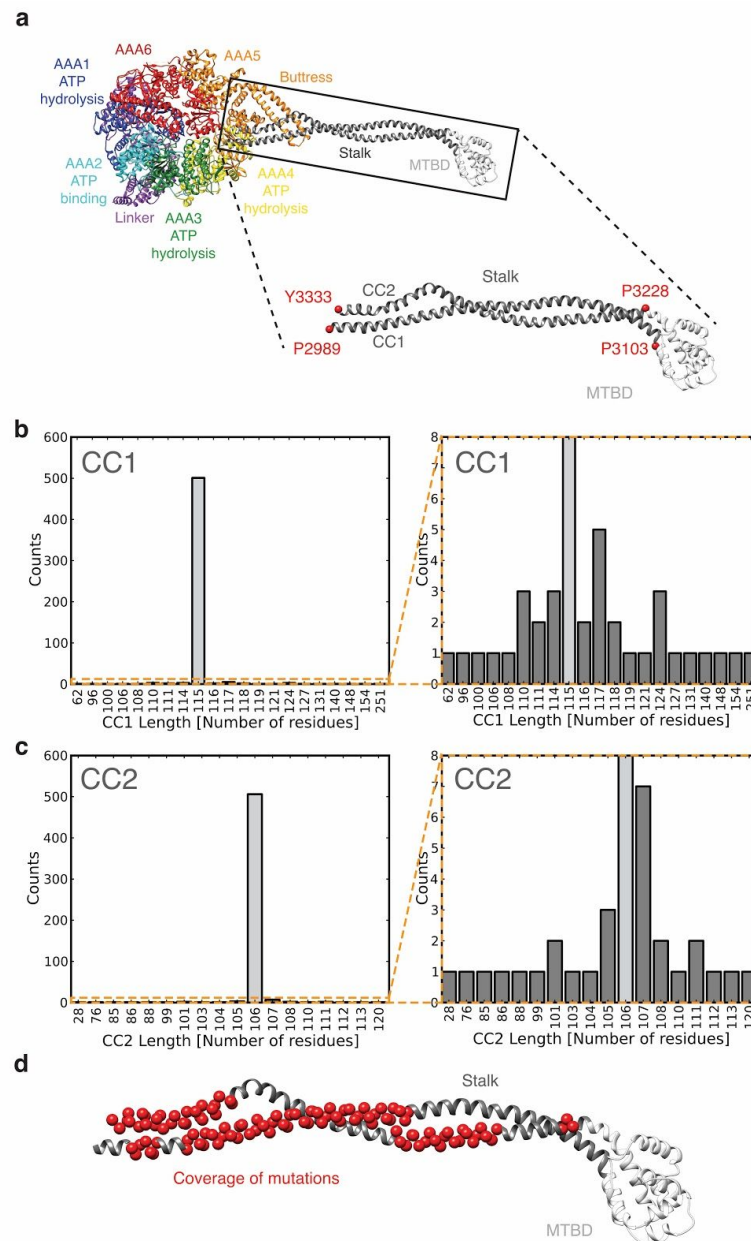


Figure 1 | Sequence analysis of the dynein stalk. (a) Structure and domain organization of the motor domain of cytoplasmic dynein (PDB: 4rh7¹²). Inset shows zoom of MTBD (white) and coiled-coil stalk (grey), which consist of two helices, CC1 and CC2. Well conserved residues, that were used as anchor points to define CC1 and CC2 in this study are depicted as red spheres. Numbering is based on yeast cytoplasmic dynein. (b) Histogram showing the length distribution of CC1 of the dynein stalk among 534 sequences that were curated as described in

Supplementary Note 1. Orange box indicates area that is shown as a zoom on the right, showing a handful of outlier sequences with different stalk lengths. **(c)** Same as in **b** but for CC2. **(d)** Coverage of all mutations generated in the yeast dynein background based on our sequence analysis. Regions of individual mutants are shown in **Supplementary Fig. 3**.

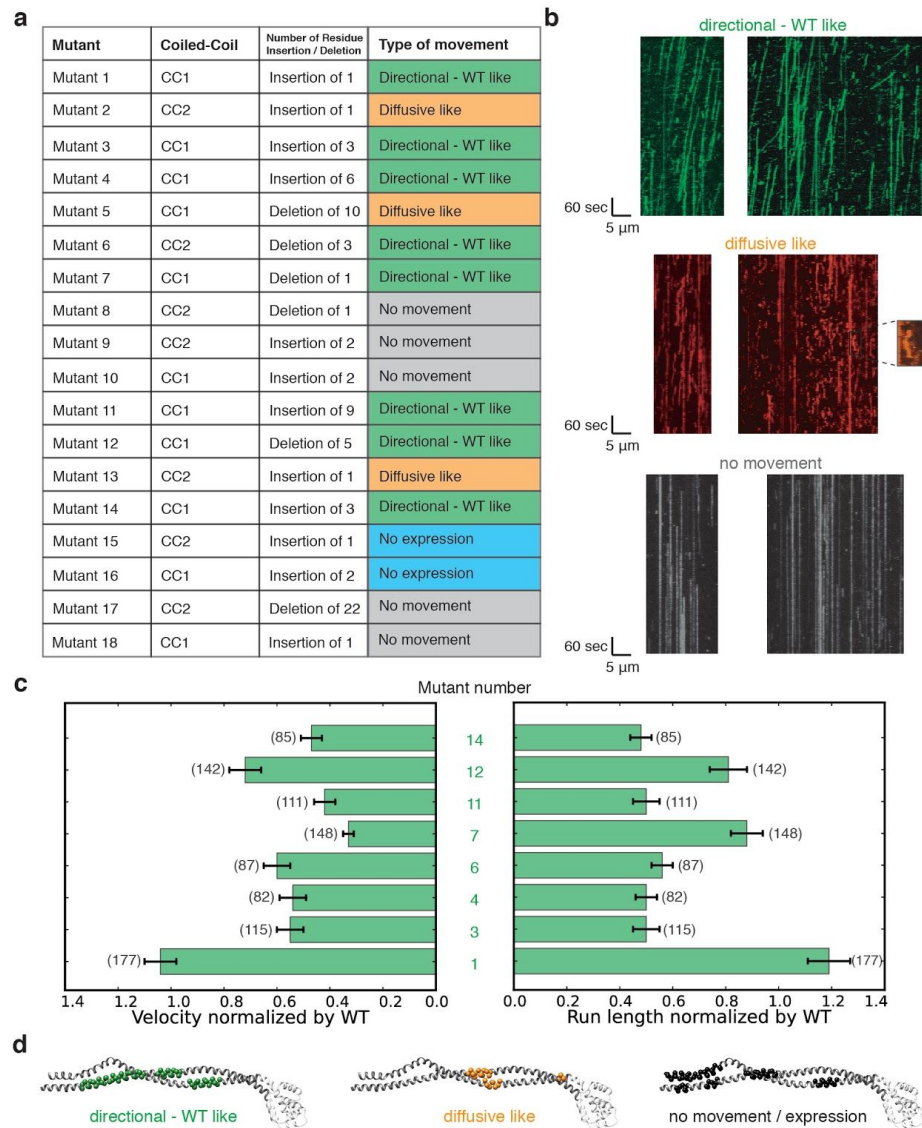


Figure 2 | Single molecule motility properties of panel of dynein stalk mutants. (a) Table showing location, number of inserted or deleted residues and motility phenotype of all 18 stalk mutants. Examples of single molecule assay results are shown in **Supplementary Fig. 4a**. Sequence information and exact position of individual mutants are shown in **Supplementary Fig 2, 3**. (b) Example kymographs for ‘Directional - WT like’ (top), ‘Diffusive like’ (middle), and ‘No movement’ (bottom). Magnified area for ‘Diffusive like’ motion shows run of single molecule. (c) Velocity and run length of ‘Directional - WT like’ motors normalized by wild-type dynein. Histograms and frequency plots for velocity and run length distributions, respectively, are shown in **Supplementary Fig. 4 b, c**. (d) Positions of insertions/deletions that showed

‘Directional - WT like’ (green), ‘Diffusive like’ (orange) movement, and ‘No movement / No expression’ (black) mapped onto the stalk. Error bars in **c** were calculated based on error propagation and number of molecules used for quantification is given in brackets. Quantification and classification in **a-c** is based on three technical repetitions.

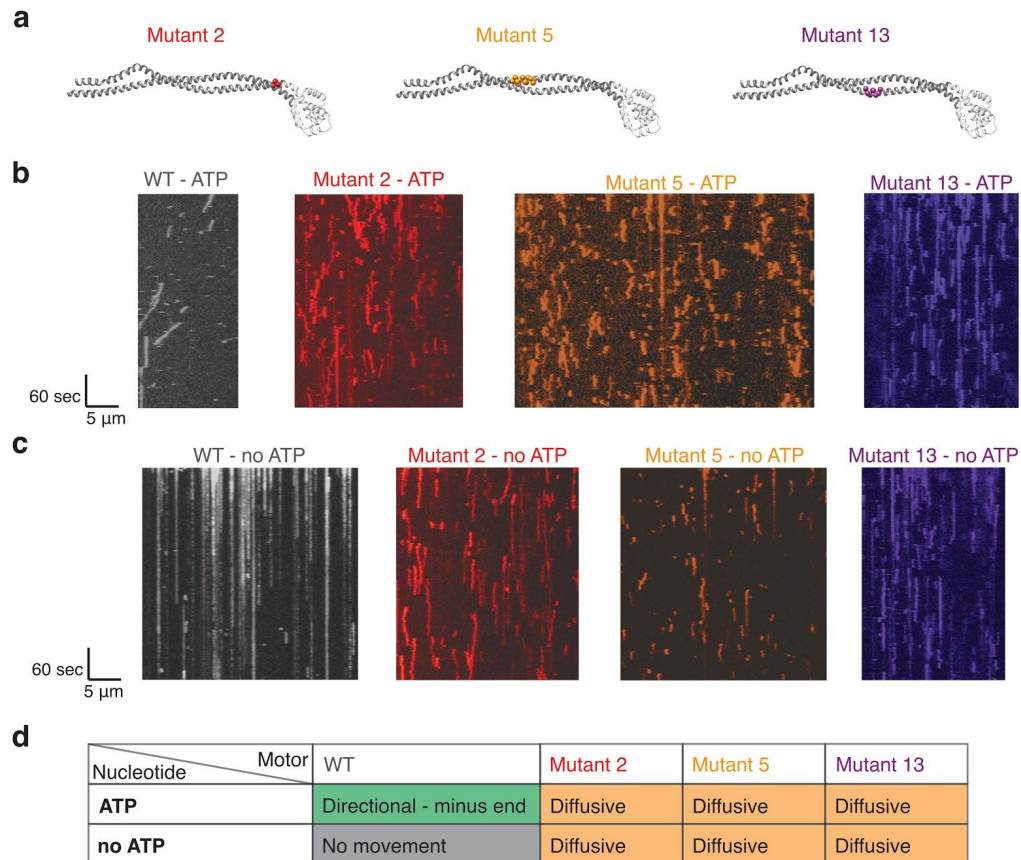


Figure 3 | Mutant 2, mutant 5, and mutant 13 show nucleotide-independent diffusive

motility. (a) Position of mutations mapped onto the structure of human cytoplasmic dynein 2 stalk (PDB: 4rh7¹²) for mutant 2, mutant 5, and mutant 13. Spheres show residues that were altered in the stalk to either create an insertion or deletion. (b) Kymographs for wild-type (grey), mutant 2 (red), mutant 5 (orange), and mutant 13 (purple) in presence of ATP and (c) without ATP. Additional kymographs are shown in **Supplementary Fig. 5**. (d) Table showing the type of movement found for wild-type, mutant 2, mutant 5, and mutant 13 in modified single molecule assay with and without ATP. Classification of type of movement is based on two repetitions of different dynein preparations. **Supplementary Movies 1-4 and 5-8** show motility of wild-type and diffusive mutants with and without ATP, respectively.

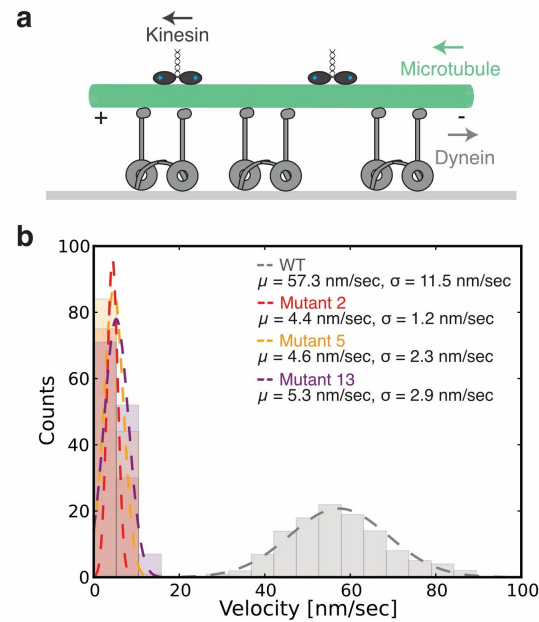


Figure 4 | Gliding assay shows slow directional movement for mutants 2, 5, and 13. (a)

Schematic of modified gliding assay. Dyneins (dark grey) are immobilized on microscope slide (light grey) and can translocate microtubule (green). Plus end directed kinesins (dark blue) move on top of microtubule to mark directionality. **(b)** Histogram of gliding velocities of wild-type (grey, n=116), mutant 2 (red, n=105), mutant 5 (orange, n=129), and mutant 13 (purple, n=130) with average velocity (μ) and its standard deviation (σ). Example movies of microtubule gliding for all four constructs are shown in **Supplementary Movies 9-12**.

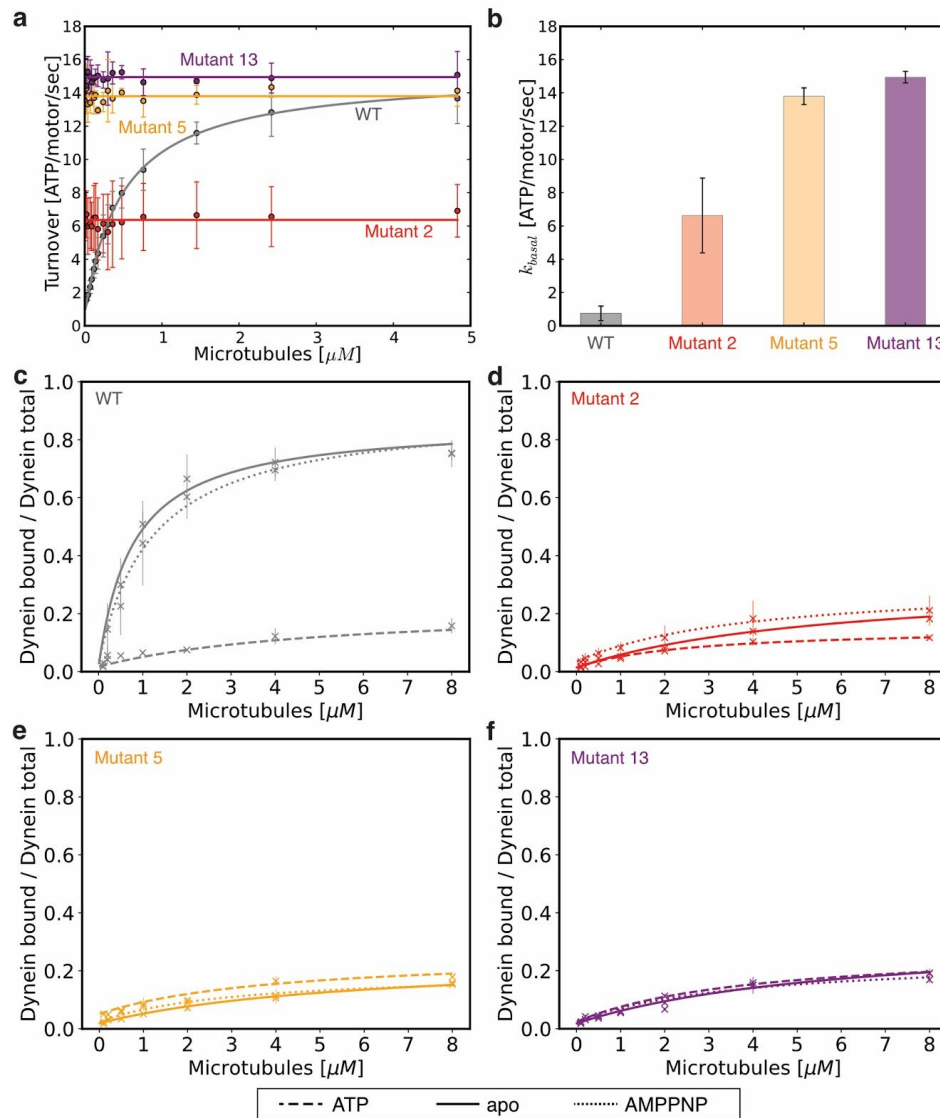


Figure 5 | Diffusive mutants show microtubule-independent, high basal ATPase activity and low affinity for microtubules. (a) Microtubule stimulated ATPase activity of wild-type (grey), mutant 2 (red), mutant 5 (orange), and mutant 13 (purple). (b) Bar plot of basal ATPase activity of wild-type (grey), mutant 2 (red), mutant 5 (orange), and mutant 13 (purple).

Microtubule affinity measured by a cosedimentation assay in the apo state (full line) and in the presence of ATP (dashed line), and AMPNP (dotted line) for (c) wild-type, (d) mutant 2, (e) mutant 5, and (f) mutant 13. Error bars in a-f show standard deviation of three repetitions of different dynein preparations. **Supplementary Table 3 and 4** show fit equation and rate quantification for ATPase data and microtubule affinity data, respectively.

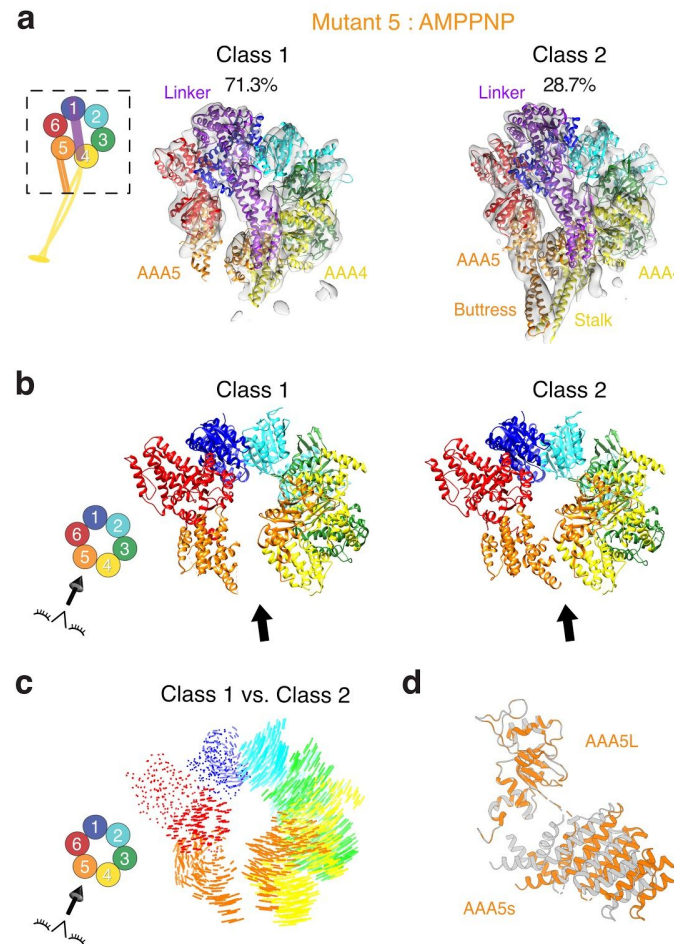


Figure 6 | Cryo-EM structure of mutant 5 in the presence of AMPPNP shows gap in the AAA ring. (a) Cryo EM reconstructions and fitted models for class 1 and class 2 resulting from 3D classification of the data. Class 1 is composed of 71.3% of all particles (left) and class 2 of 28.7% of all particles (right). The cryo-EM density map for both classes is shown as a semi-transparent surface with a fitted model (fit as described in methods) as cartoon. Color coding of domains is the same as for **Fig. 1**. Left: schematic of monomeric dynein construct, box indicates region that was resolved in the cryo-EM maps. (b) Cartoon representation of models for both classes. Black arrow indicates the position of the gap between AAA5L and AAA5s in class 1. Left: schematic indicates the point-of-view. (c) Visualization of interatomic distances between class 1 and class 2 as shown in (b) after alignment on AAA1L. Left: schematic indicates the point-of-view. (d) Movements between the large and small domains of AAA5 between class 1 (orange) and class 2 (grey). The large domain of AAA5 is aligned.

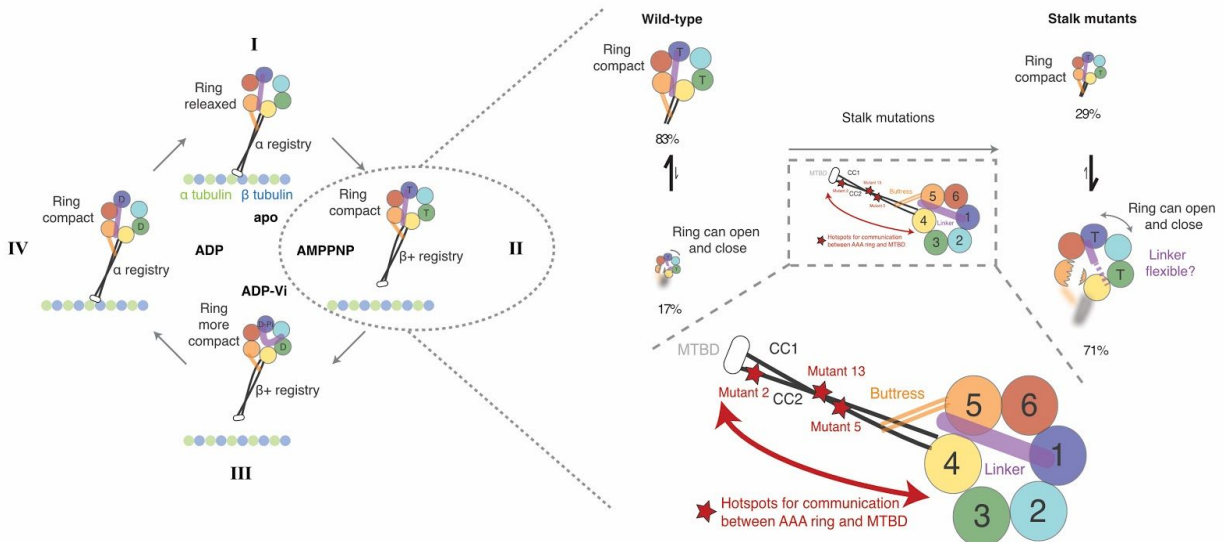


Figure 7 | A model for communication between ring and MTBD during the mechanochemical cycle of dynein. Conformational changes in the AAA ring, the linker, and the stalk of dynein during different nucleotide states based on crystal structures and EM reconstructions^{11–13,18} (left). (I) In the apo state dynein is bound to the MT and the stalk has been shown to be in the α registry²¹. The ring is in a relaxed conformation and the linker is docked. (II) When AMPPNP is bound, the linker remains docked and the ring is more compact than in the apo state. The stalk transitions to the β registry and the affinity of the motor for microtubules is weakened. (III) In the presence of ADP-Vi the linker bends so that its N-terminus is closer to AAA2 and AAA3 and the ring is even more compact. Furthermore a kink in CC2 of the stalk can be observed. (IV) When only ADP is bound to AAA1 and AAA3, the linker is seen in a straight conformation and the ring is a little less compact. Moreover, the stalk changes back to the α registry.

For the AMPPNP state of wild-type dynein a minor (17%) and a major conformation (83%) can be adopted. The major conformation is as previously reported¹⁸ with the ring in a compact state, while in the minor conformation the ring is likely in a relaxed conformation, as evidenced by weak density in the region of AAA5. For mutant 5 we observe a shift in equilibrium where the relaxed ring with a break at AAA5 is the major conformation (71%) and the compact state of the ring is less prominent (29%).

References

1. Vale, R. D. The molecular motor toolbox for intracellular transport. *Cell* **112**, 467–480 (2003).
2. Vallee, R. B., Williams, J. C., Varma, D. & Barnhart, L. E. Dynein: An ancient motor protein involved in multiple modes of transport. *J. Neurobiol.* **58**, 189–200 (2004).
3. Kiyomitsu, T. & Cheeseman, I. M. Cortical dynein and asymmetric membrane elongation coordinately position the spindle in anaphase. *Cell* **154**, 391–402 (2013).
4. Roberts, A. J., Kon, T., Knight, P. J., Sutoh, K. & Burgess, S. A. Functions and mechanics of dynein motor proteins. *Nat. Rev. Mol. Cell Biol.* **14**, 713–726 (2013).
5. Pfister, K. K. *et al.* Genetic analysis of the cytoplasmic dynein subunit families. *PLoS Genet.* **2**, e1 (2006).
6. Vallee, R. B., McKenney, R. J. & Ori-McKenney, K. M. Multiple modes of cytoplasmic dynein regulation. *Nat. Cell Biol.* **14**, 224–230 (2012).
7. Kardon, J. R. & Vale, R. D. Regulators of the cytoplasmic dynein motor. *Nat. Rev. Mol. Cell Biol.* **10**, 854–865 (2009).
8. McKenney, R. J., Huynh, W., Tanenbaum, M. E., Bhabha, G. & Vale, R. D. Activation of cytoplasmic dynein motility by dynactin-cargo adapter complexes. *Science* **345**, 337–341 (2014).
9. Schlager, M. A., Hoang, H. T., Urnavicius, L., Bullock, S. L. & Carter, A. P. In vitro reconstitution of a highly processive recombinant human dynein complex. *EMBO J.* **33**, 1855–1868 (2014).
10. Burgess, S. A., Walker, M. L., Sakakibara, H., Knight, P. J. & Oiwa, K. Dynein structure and power stroke. *Nature* **421**, 715–718 (2003).

11. Carter, A. P., Cho, C., Jin, L. & Vale, R. D. Crystal structure of the dynein motor domain. *Science* **331**, 1159–1165 (2011).
12. Schmidt, H., Zalyte, R., Urnavicius, L. & Carter, A. P. Structure of human cytoplasmic dynein-2 primed for its power stroke. *Nature* **518**, 435–438 (2015).
13. Kon, T. *et al.* The 2.8 Å crystal structure of the dynein motor domain. *Nature* **484**, 345–350 (2012).
14. Schmidt, H., Gleave, E. S. & Carter, A. P. Insights into dynein motor domain function from a 3.3-Å crystal structure. *Nat. Struct. Mol. Biol.* **19**, 492–7, S1 (2012).
15. Cho, C., Reck-Peterson, S. L. & Vale, R. D. Regulatory ATPase sites of cytoplasmic dynein affect processivity and force generation. *J. Biol. Chem.* **283**, 25839–25845 (2008).
16. Kon, T., Nishiura, M., Ohkura, R., Toyoshima, Y. Y. & Sutoh, K. Distinct functions of nucleotide-binding/hydrolysis sites in the four AAA modules of cytoplasmic dynein. *Biochemistry* **43**, 11266–11274 (2004).
17. Bhabha, G., Johnson, G. T., Schroeder, C. M. & Vale, R. D. How Dynein Moves Along Microtubules. *Trends Biochem. Sci.* **41**, 94–105 (2016).
18. Bhabha, G. *et al.* Allosteric communication in the dynein motor domain. *Cell* **159**, 857–868 (2014).
19. DeWitt, M. A., Cypranowska, C. A., Cleary, F. B., Belyy, V. & Yildiz, A. The AAA3 domain of cytoplasmic dynein acts as a switch to facilitate microtubule release. *Nat. Struct. Mol. Biol.* **22**, 73–80 (2015).
20. Vale, R. D. & Milligan, R. A. The way things move: looking under the hood of molecular motor proteins. *Science* **288**, 88–95 (2000).
21. Kon, T. *et al.* Helix sliding in the stalk coiled coil of dynein couples ATPase and microtubule binding. *Nat. Struct. Mol. Biol.* **16**, 325–333 (2009).

22. Imamula, K., Kon, T., Ohkura, R. & Sutoh, K. The coordination of cyclic microtubule association/dissociation and tail swing of cytoplasmic dynein. *Proc. Natl. Acad. Sci. U. S. A.* **104**, 16134–16139 (2007).
23. Gibbons, I. R. *et al.* The affinity of the dynein microtubule-binding domain is modulated by the conformation of its coiled-coil stalk. *J. Biol. Chem.* **280**, 23960–23965 (2005).
24. Redwine, W. B. *et al.* Structural basis for microtubule binding and release by dynein. *Science* **337**, 1532–1536 (2012).
25. Carter, A. P. *et al.* Structure and functional role of dynein's microtubule-binding domain. *Science* **322**, 1691–1695 (2008).
26. Oiwa, K. & Sakakibara, H. Recent progress in dynein structure and mechanism. *Curr. Opin. Cell Biol.* **17**, 98–103 (2005).
27. Shima, T., Kon, T., Imamula, K., Ohkura, R. & Sutoh, K. Two modes of microtubule sliding driven by cytoplasmic dynein. *Proc. Natl. Acad. Sci. U. S. A.* **103**, 17736–17740 (2006).
28. Nishikawa, Y., Inatomi, M., Iwasaki, H. & Kurisu, G. Structural Change in the Dynein Stalk Region Associated with Two Different Affinities for the Microtubule. *J. Mol. Biol.* **428**, 1886–1896 (2016).
29. Gee, M. & Vallee, R. The role of the dynein stalk in cytoplasmic and flagellar motility. *Eur. Biophys. J.* **27**, 466–473 (1998).
30. Katoh, K., Misawa, K., Kuma, K.-I. & Miyata, T. MAFFT: a novel method for rapid multiple sequence alignment based on fast Fourier transform. *Nucleic Acids Res.* **30**, 3059–3066 (2002).
31. Alva, V., Nam, S.-Z., Söding, J. & Lupas, A. N. The MPI bioinformatics Toolkit as an integrative platform for advanced protein sequence and structure analysis. *Nucleic Acids Res.* **44**, W410–5 (2016).

32. Reck-Peterson, S. L. *et al.* Single-molecule analysis of dynein processivity and stepping behavior. *Cell* **126**, 335–348 (2006).
33. DeWitt, M. A., Chang, A. Y., Combs, P. A. & Yildiz, A. Cytoplasmic dynein moves through uncoordinated stepping of the AAA+ ring domains. *Science* **335**, 221–225 (2012).
34. Yildiz, A. & Vale, R. D. Tracking Movements of the Microtubule Motors Kinesin and Dynein Using Total Internal Reflection Fluorescence Microscopy. *Cold Spring Harb. Protoc.* **2015**, db.prot086355 (2015).
35. Tomishige, M., Stuurman, N. & Vale, R. D. Single-molecule observations of neck linker conformational changes in the kinesin motor protein. *Nat. Struct. Mol. Biol.* **13**, 887–894 (2006).
36. Toropova, K. *et al.* Lis1 regulates dynein by sterically blocking its mechanochemical cycle. *Elife* **3**, (2014).
37. Waterhouse, A. M., Procter, J. B., Martin, D. M. A., Clamp, M. & Barton, G. J. Jalview Version 2—a multiple sequence alignment editor and analysis workbench. *Bioinformatics* **25**, 1189–1191 (2009).
38. Mori, T., Vale, R. D. & Tomishige, M. How kinesin waits between steps. *Nature* **450**, 750–754 (2007).
39. Tomishige, M., Stuurman, N. & Vale, R. D. Single-molecule observations of neck linker conformational changes in the kinesin motor protein. *Nat. Struct. Mol. Biol.* **13**, 887–894 (2006).
40. Edelstein, A., Amodaj, N., Hoover, K., Vale, R. & Stuurman, N. Computer control of microscopes using µManager. *Curr. Protoc. Mol. Biol.* **Chapter 14**, Unit14.20 (2010).
41. Schneider, C. A., Rasband, W. S. & Eliceiri, K. W. NIH Image to ImageJ: 25 years of image analysis. *Nat. Methods* **9**, 671–675 (2012).

42. Aitken, C. E., Marshall, R. A. & Puglisi, J. D. An oxygen scavenging system for improvement of dye stability in single-molecule fluorescence experiments. *Biophys. J.* **94**, 1826–1835 (2008).
43. Suloway, C. *et al.* Automated molecular microscopy: the new Legimon system. *J. Struct. Biol.* **151**, 41–60 (2005).
44. Mastronarde, D. N. Automated electron microscope tomography using robust prediction of specimen movements. *J. Struct. Biol.* **152**, 36–51 (2005).
45. Voss, N. R., Yoshioka, C. K., Rademacher, M., Potter, C. S. & Carragher, B. DoG Picker and TiltPicker: software tools to facilitate particle selection in single particle electron microscopy. *J. Struct. Biol.* **166**, 205–213 (2009).
46. Lander, G. C. *et al.* Appion: an integrated, database-driven pipeline to facilitate EM image processing. *J. Struct. Biol.* **166**, 95–102 (2009).
47. Scheres, S. H. W. RELION: implementation of a Bayesian approach to cryo-EM structure determination. *J. Struct. Biol.* **180**, 519–530 (2012).
48. Punjani, A., Rubinstein, J. L., Fleet, D. J. & Brubaker, M. A. cryoSPARC: algorithms for rapid unsupervised cryo-EM structure determination. *Nat. Methods* **14**, 290–296 (2017).
49. doi:10.1101/061960
50. Zhang, K. Gctf: Real-time CTF determination and correction. *J. Struct. Biol.* **193**, 1–12 (2016).
51. Pettersen, E. F. *et al.* UCSF Chimera—A visualization system for exploratory research and analysis. *J. Comput. Chem.* **25**, 1605–1612 (2004).
52. Adams, P. D. *et al.* PHENIX: a comprehensive Python-based system for macromolecular structure solution. *Acta Crystallogr. D Biol. Crystallogr.* **66**, 213–221 (2010).